Complex structure models mutated anode/cathode electrodes for improving large-scale battery designs

H. Khalifa[1#], M. A. Shenashen[1,#] A. Reda[1], M. M. Selim[2].A. Elmarakb[3], S. A. El-Safty[1*]*

[1] National Institute for Materials Science (NIMS), Sengen 1-2-1, Tsukuba, Ibaraki 305-0047, Japan. E-mail: sherif.elsafty@nims.go.jp

[2] Prince Sattam Bin Abdulaziz University, P. O. Box 173, Al-Kharj 11942, Saudi Arabia

[3] Department of Mechanical & Construction Engineering, Faculty of Engineering and Environment, Northumbria University, Newcastle Upon Tyne, NE1 8ST, UK.

E-mail: ahmed.elmarakbi@northumbria.ac.uk

[#] These authors contributed equally to this work

[#] Current Address: Department of Physics, Faculty of Science, Damanhur University, Damanhur, Egypt (H. Khalifa) & [#] Current Address: Department of Petrochemical, Egyptian Petroleum Research Institute, Cairo 11727, Egypt (M.A. Shenashen).

ABSTRACT: We fabricate diverse geometric scales of lithium-ion battery (LIB) pattern assemblies in CR2032-circular coin designs by using complex building-block (CBB) anode/cathode electrodes as hierarchical models. The CBB anode/cathode electrode architectonics are designed with multiple complex hierarchies, including uni-, bi-, and tri-modal morphologies, multi-directional configurations, geometrical assemblies oriented in nano-/micro-scale structures, and surface mesh topologies, which allow us to leverage half- and full-cell CBB–LIB models. The CBB–LIB CR2032-circular coin designs have a Coulombic efficacy of ~99.7% even after 2000th lithiation/delithiation (discharge/charge) cycles, an outstanding battery energy density of 154.4 Wh/kg, and a specific discharge capacity of 163.6 mAh/g from 0.8 V to 3.5 V and at 0.1 C. The architectonic configurations and geometrics of the modulated full-cell CBB–LIB CR2032-circular designs play key roles in creating sustainable, full-scale CBB-mutated-LIBs with continuous and non-resisted surface transports and in achieving a sensible distribution of electron/Li^+ ions. With hierarchical uni-, bi-, and tri-modal complexities, a dense collar packing f anode/cathode CBB-mutated-LIB pouch-type sets in stacked layers can facilitate a rational design of CBB-pouch-type LIBs. Our CBB-mutated pouch-type LIB models have a sustainable Li^+ ion-transport along multi-complex CBB-surfaces, substantial areal discharging capacity, and excellent volumetric- and gravimetric-cell energy densities and specific capacitances that fulfill the powerful force-driving range and tradeoff requirements in electric vehicle applications.

Keywords: complex building-blocks (CBBs), half- and full-cell LIBs, CBB-pouch-type battery, reversible recovery, rate capabilities, gravimetric and volumetric cell energy densities

Introduction

The current demand for green energy has increased as a result of the rapid depletion of fossil fuel reserves.[1-4] Accordingly, many studies have explored sustainable energy sources and proposed electro-chemical storage/conversion techniques.[1,2] The progress of rechargeable LIBs as clean and sustainable sources of green energy for modern engineering electronic devices has received much interest. [1,5] LIBs are also known as one of the most efficient energy technologies for electric vehicles (EVs). These batteries can be manufactured in countless sizes and forms that can be plugged into spaces. LIBs have been classified as zero-emission and low-carbon society. LIBs have provided the battery technology with volumetric- and gravimetric-cell energy densities and specific capacitances.[6-9] Recently, the progress of hierarchical-structure with multi-directional configurations, architectonics, and geometrics can lead to incorporate anode/cathode electrodes and to ensure a safe manufacturing of LIB models while maintaining their highly efficient energy and power densities. [8-11]

To achieve such aim, a controlled fabrication of hierarchical anode/cathode electrode materials with high structural orientation stability, low economic cost, high safety, and eco-friendly qualities is crucial.[5-11] Researchers have also called for the development of nano-scale architectonic-materials-based electrodes to replace hazardous Li–MOx substances, such as $LiCoO_2$, $LiNiO_2$, or $LiMn_2O_4$, in designing LIBs. Among the available poly-anion-type composites, composite phosphor olivine-structured $LiXPO_4$ (LXPO, where X is a transition metal type) cathode materials with a theoretical specific discharging capacity (~ 170 $mAhg^{-1}$).[10-12] Among these materials, $LiFePO_4$ (LFPO) has distinctive semantics that support its application as a cathode in the manufacturing of rechargeable LIBs. [12-14] LFPO–cathode electrodes have also been effectively used in manufacturing rechargeable LIBs because of their stable crystal structures and surface

topologies, high safety, low cost, and environment-friendly qualities. [12-14] However, LFPO-based cathode materials have obvious disadvantages that limit their use electrode-designed LIB applications, including their poor reversibility and capability rates, weak conductivity and electron diffusivity, and slow electron/Li^+ ion transport along LFPO-solid/electrolyte interfaces. [15-18] Therefore, several strategies for designing hierarchical cathode electrodes have been developed to overcome the aforementioned limitations and to enhance the conductivity and facilitate the durable transport of Li^+ ions. [19, 20] Several strategies for fabricating multifunctional cathode electrodes based nanomaterials and its hierarchical structures have also been applied for energy storage/conversion designs. These strategies were used for modification surface of electrodes such as (i) modifying their nano-/micro-structured surfaces and (ii) decorating these materials with supervalent metal composites, highly conductive materials, highly exposed facet surfaces, and hierarchically structured configurations. [19-33] The synthesis of potential LFPO-–cathode electrode composites with high surface heterogeneity and highly conductive carbon layers was controlled by using woven decoration methods or the surface-doped strategy. [1, 5,6, 8] The development of hierarchical LFPO-cathode models with 3D multi-functional complex architectonics and a mixture of heterogeneous surface composites can facilitate the fabrication of LIB pattern assemblies with diverse geometric scales.

Polymorphous metal oxides, such as TiO_2 (TO), have promising use in manufacturing rechargeable LIBs. TO-based materials have shown excellent behavior as electro-active host matrices for the intercalation of Li^+ ions during charging/discharging processes. [34] TO-based anode electrode structures have certain advantages, including their low economic cost, high safety, non-production of harmful byproducts, zero toxicity, high reversibility/capability rate, and high stability after multiple cycles. [34- 37] TO crystal structures have eight polymorphs, including anatase,

rutile, brookite, bronze, ramsdellite, hollandite, columbite, and baddeleyite ordering arrangements. [38- 46] Anatase–TO structures (ATO) also have a prominent anode capability in half-scale LIB designs. Specifically, the crystal orientation of ATO effectively promotes surface mobility to improve electron/Li^+ ion inflow. [40, 47] Despite having a high operating voltage and a theoretical discharge capacity that is close to that of graphite anode (335 $mAhg^{-1}$), ATO lacks a powerful force-driving range, thereby failing the to satisfy the requirements in EV applications. [34] The distinct electron transportation and Li^+ ion diffusion kinetics of anode surface interfaces during multiple lithiation/delithiation cycles of LIBs play key roles in improving electric conductivity. In addition, hierarchical anode complex architectures and their corresponding model alignments must be developed in LIB designs.

In this paper, we fabricate (i) complex building block (CBB)-mutated anode/cathode electrodes, (ii) diverse models of half-/full-scale CBB–LIB coin cell designs, and (iii) CBB-pouch-type LIB sets. Known for their hierarchical complexity, CBB anode/cathode electrode architectonics are designed with complex uni-, bi-, and tri-modal-hierarchy morphologies, multi-directional configurations, geometrical assemblies oriented in nano- and micro-structures, and mesh-like surface topologies as well as contain a large number of bristles, corrugations, and tercets that are woven into tightly folded winglets to enable the engineering of LIBs across diverse geometric scales. A sustainable engineering of CBB–LIB can lead to a high Coulombic efficacy of 97.7% even after 2000^{th} lithiation/delithiation (discharge/charge) cycles, a specific discharge capacity of 163.6 mAh/g, and energy density battery of 154.4 Wh/kg from 0.8 V to 3.5 V and at 0.1 C. The CBB–LIB sustainability of mimic complex architectonics in the developed anode/cathode electrodes can also lead to non-resisted surface mobility, sensible distribution dynamics of electron/Li^+ ions, and innumerable lithiation/delithiation (discharge/charge) cycling processes

(>>2,000 cycles). Scalable CBB-pouch-type LIBs are designed through a dense collar packing of CBB-mutated LIB sets in continuously connected and stacked layers. CBB-pouch-type LIBs have a sustainable rate capability, high energy density, excellent charging/discharging performance, and sufficient areal discharge capacity to gratify the tradeoff and energy storage demands in LIB manufacturing.

Experimental sets

Synthesis of 3D CBB–LFPO-hierarchy as cathode material architectonics

Three hierarchical-structure models of 3D CBB–LFPO cathodic architectonics were fabricated with variable uni-, bi-, and tri-modal hierarchies, multi-directional configurations, geometrical assemblies oriented in nano-/micro-scale structures, and surface mesh topologies. These architectonics have various morphological shapes, such as soaring eagles (SE), Australian Bryozoan (AB) hornwracks, and stackable complex structures with rectangular cube blocks (CC), and were manufactured while simultaneously controlling the hydrothermal growth of iron Fe(III)–anion precursor types and the composition synthesis conditions at 170 °C for 12 h. Variable 3D CBB–LFPO cathodic material architectonics, including those with SE, AB, and CC morphologies, were synthesized by controlling the reducing potential of additive iron–anion precursors, such as iron chloride ($FeCl_3$), iron fluoride (FeF_3), and iron nitrate nonahydrate ($Fe(NO_3)_3.7H_2O$), for the synthesis components. The relatively high reducing potential of $Fe^{(III)}$–anion precursors reduces in the following order of NO_3^- - > F^- - > Cl^- -anion, leading to direct the formation of CC, AB, and SE geometrics, respectively. For instance, the low reducing power of the Cl^- anion can efficiently control the anisotropic nucleation growth of complex SE particles in stable thermodynamic aggregation and slow-rate kinetics.

To improve the simplicity and scalability of the synthesis protocol of cathode materials, variable 3D CBB–LFPO geometric units with SE, AB, and CC morphologies were designed via the mechanistic control of hierarchical cathode material models. The designing was divided into three sub-processes, namely, (i) performing a growth-time-dependent scale synthesis, (ii) identifying the chemical composition ratios of components, and (iii) reducing the potential of iron–anion precursors (i.e., Fe(III)–anions, such as Cl^{-}, F^{-}, and NO_3^{-}). Among the controllable synthesis conditions of LFPO geometrics, adding the variable precursors of $FeCl_3$, FeF_3, and $Fe(NO_3)_3$ as synthesis components significantly affects the fabrication of 3D LFPO structures with SE, AB, and CC morphologies, respectively. The final LFPO molar ratio of the synthesized components (Li–hydroxide ($LiOH.H_2O$): Fe(III)–anion precursor sources: P (H_3PO_4)) in the experiment was fixed at 3:1:1. Two separate solutions of Fe(III)–source and H_3PO_4 components were prepared in a composition containing 5 mL H_2O, 2.5 mL C_2H_5OH (ethanol), and 0.003 mL $(CH_2OH)_2$ (ethylene glycol) and stirred for 30 minutes. Another $LiOH.H_2O$ solution was prepared in a mixture containing 10 mL H_2O, 5 mL C_2H_5OH, and 0.006 mL $(CH_2OH)_2$ and was mixed under magnetic stirring for 1 hour at 30 °C. The $LiOH.H_2O$/Fe(III)/H_3PO_4 solution was mixed under magnetic stirring for 6 hours at pH 7. The composite solution was hydrothermally treated at 170 °C for 12 hours in autoclaves. The 3D CBB–LFPO products with SE, AB, and CC morphologies were collected, washed, dried, and calcined at high-temperature (600 °C for 6 h).

Synthesis of 3D CBB–ATO anode material architectonics

To synthesize 3D CBB–ATO materials with multi-hole spherulites-like reef ball vortices (CBB–HS morphology) anodic materials, a 1 mL homogenous titanium isopropoxide (TIP) solution was prepared in a 20 mL HCl solution (2M) by continuous stirring for 6 h. Aftterward, 3 mL H_2O_2 (30%) was mixed with TIP solution contents and stirred for 1 hour at pH 9.2. The mixture was

then transferred to an autoclave and treated at 170 °C for 12 hours. The 3D CBB–HS geometric spherulites were collected, washed, and calcined at high temperature (at 600 °C for 2 hours).

Synthesis of 3D CBB–HS@carbon (C) and 3D CBB–LFPO@C architectonics

Carbon layers with 1-5 nm-thicknesses were post-decorated the surface of 3D CBB–HS anode and 3D CBB–LFPO cathodes. The post-carbon grafting coated the exterior/outer surfaces of the hierarchical CBB–anode/–cathode models with carbon layers. 3D CBB–LFPO, including SE, AB hornwracks, CC cathode, and CBB–HS anode materials, was then dispersed into a glucose-solution (G) (5 w/w%) under ultrasonic conditions for 20 min. The final CBB-LFPO/G or CBB-HS/G mixture domains were stirred vigorously in autoclaves for 20 min before they were treated under irradiation conditions (at 80 °C for 30 min). The collected CBB-cathodic and CBB-anodic materials were washed and kept in an electric oven (at 55 °C for 24 hours), before they were treated thermally at 600 °C for 2 hours under an argon atmosphere.

Fabrication of working 3D CBB-HS@C anode (negative (N)) and 3D CBB-LFPO@C cathode (positive (P)) electrodes

Working 3D CBB-HS@C anode (negative (N)) and 3D CBB-LFPO@C cathode (positive (P)) electrodes were fabricated by incorporating anodic and cathodic active materials into Cu-foil (8 μm thickness) and Al-foil (10 μm thickness) films, respectively. In a typical synthesis procedure, the active anodic and cathodic materials were blended separately with polyvinylidene fluoride (PVDF) and carbon-black (C-black) with fraction composition ratios of 0.75: 0.15: 0.10 (cathodic or anodic active materials: C-black: PVDF linker) (see supporting information S1 and Fig. S1). Afterward, an N-methyl-2-pyrrolidone solvent was mixed and stirred for 1 hour to create cathode or anode slurries. The P-(3D-LFPO@C) cathode and N-(HS@C) anode working electrodes were then fabricated by the grafting process. The active slurries of the cathodic and anodic materials

were modified Al-disc (10 μm thickness) and Cu-disc films (8 μm thickness), respectively. The designed P-(3D-LFPO@C) cathode and N-(HS@C) anode disc-like films were kept at 70 °C for 12 hours to dry and compressed between twin rollers. This electrode compression process produced electrochemical experiment sets with the following key attributes: (i) a dense packing and well-defined incorporation of electrode active material hierarchies into Al- and Cu-film surface coverage, (ii) reducing the number of cracks and voids between the CBB-LFPO@C P-cathode and CBB-HS@C N-anode materials and surface electrodes, and (iii) enhancing the diffusivity along the entire electrode surfaces. In general, the compression enhances the electric conductivity and guarantees a continuous Li^+ ion mobility along the entire surface of P- and N-electrodes. The actively loaded geometric materials of both 3D CBB-HS@C- and CBB-LFPO@C-integrated Cu- and Al-film surfaces were 6.71 mg/cm^2 and 14.82 mg/cm^2, respectively, thereby enabling the fabrication of effective CBB-HS@C (i.e., CBB-N) anode and CBB-LFPO@C (i.e., CBB-P) cathode electrodes (see supporting information S1 and S2).

Constituents of half- and full-cell CBB–LIB CR2032-circular coin designs

CR2032-circular coin cells were used to design half- and full-cell CBB-mutated-LIBs. The components used to create CBB–LIB CR2032-circular coin designs include (i) a 16 mm circular-shaped Li-ship (as the reference/counter electrode), (ii) coin-shaped CBB-P and CBB-N discs (as the working electrodes) of CBB-LFPO@C- and CBB-HS@C-integrated Al- and Cu-film surfaces, respectively, (iii) a 20 mm circular separator formed from a micro-porous polymeric membrane, and (iv) a 1 M highly conductive electrolyte solution containing $LiPF_6$ /$(CH_2O)_2CO$ (ethylene carbonate)/$C_5H_{10}O_3$ (diethyl carbonate) mixture. The CBB–LIB CR2032-circular coin cell had a total mass of ~ 3.5 g when all specific components and packaging contents were included (Fig. S1).

Before performing electrochemical experiments on the CR2032-type coin cell in half- or full-scale LIB models, a crimper machine was used for mechanical pressing of the coin-cell models. The mechanical process of the CBB-LIB CR2032-type coin cell was implemented into glove-box under argon (Ar) atmosphere. The prepared CR20XX coin-cell battery and its components were stored one day before the electrochemical examination. The quasi-steady state of the CBB–LIB CR2032-type coin cell was used to improve (i) active CBB-LFPO@C and CBB-HS@C stability onto P- and N-working electrode surfaces, and (ii) thermodynamic system and internal equilibrium between highly conductive electrolyte solution and solid N- or P- surface electrodes.

In addition to guaranteeing the safety and maintaining the excellent electrochemical performance of CBB–LIB CR2032-circular coin designs and the dense packing of circular-shaped electrodes, separator films, and package contents of CBB–LIB CR2032-circular coin cells, a mechanical processing control was implemented to enhance non-resisted electrode capability, retain the highly electrical conductivity along the interfaces formed between the CBB-LFPO@C cathode/CBB-HS@C anode electrodes and the highly conductive electrolyte solution, and stabilize the mobility and diffusion kinetics of electron/Li^+ ions along the CBB–LIB CR2032 circular-type coin cells.

Fabrication of CBB-pouch-type LIB cell batteries

To study the large-scale control of CBB-pouch-type LIBs fabrication, multiple sets of full-cell anode/cathode electrodes were grouped and tightly packed in series following a dense collar packing protocol. In this protocol, CBB–SE@C cathode and CBB–HS@C anode electrodes were continuously attached and stacked in layers (Fig. S2). A rational control of well-packed and densely stacked layers of several P-//N-electrodes was contiguously designed in series to obtain CBB-pouch-type LIBs with substantial cell-battery energy densities (i.e., gravimetric/volumetric

performances), high areal capacity, and favorable sustainability. Stacked layers of CBB–HS@C anode (CBB–N electrode)//CBB–SE@C cathode (CBB–P electrode) were configured to have 5 to 6 layers, with each layer having 10 sides. The active mass components of the CBB–HS@C anode (N-electrode) and CBB-SE@C cathode (P-electrode) along the CBB-pouch-type LIB constituents were 0.958 g and 2.223 g, respectively. The mass fractions of the CBB–HS@C anode slurry-supported Cu-foils (N-electrode) and CBB–LFPO@C cathode slurry-supported Al-foils (P-electrode), as components of a single CBB–LIB pouch-type battery, were approximately 21.3% and 49.4%, respectively. Figure S2 presents a schematic diagram of the individual components and mass fractions of hierarchical complex CBB-pouch-type LIB battery models.

The stacked and connected CBB–HS@C anode (N-electrode)//CBB–SE@C cathode (P-electrode) layer in the CBB-pouch-type LIB models was designed these dimensions (5.5 cm long, 3.5 cm wide, and ~0.25 m to 0.3 cm thick). Therefore, the total area (cm^2) and mass stacking (mg/cm^2) of the packed CBB–HS@C anode (N-electrode)//CBB–SE@C cathode (P-electrode) in a CBB-pouch-type battery were 143 cm^2 and 150 cm^2 and 6.71 mg/cm^2 and 14.82 mg/cm^2, respectively (see supporting information S2 and S3). Accordingly, the areal capacities of both CBB–HS@C anode (N) and CBB–SE@C cathode (P) electrodes in the configuration of the CBB-pouch-type LIB cell at 0.1 C were 1.124 mAh/cm^2 and 2.48 mAh/cm^2, respectively. The control sets of the experimental key factor conditions and dimensions as well as the mass components of CBB-pouch-type LIB constituents influenced the production of excellent gravimetric and volumetric cell energy densities while satisfying the tradeoff requirements for EVs (see Scheme 1, and supporting information S2, and S3).

Results and Discussion

Fabrication of 3D CBB-anode/-cathode architectonic electrodes

The integration of hierarchical CBB-engineering models into anode/cathode electrodes enables the fabrication of diverse scales of LIB pattern assemblies. Meanwhile, the CBB-structures-modulated anode/cathode electrodes enable the assembly of LIB CR2032-circular coin designs with multiple architectonic configurations, geometrics, and surface mesh topologies. The CBB–anode was fabricated with ATO@C multi-hole spherulites-like reef ball vortices (CBB–HS@C). In addition, variable geometric CBB-LFPO@C units, such as CBB–SE@C, CBB–AB@C, and CBB–CC@C architectures, were decorated with N-cathode surfaces. Diverse alignment scales of LIB pattern assemblies were designed by using these CBB–anode/–cathode geometric electrodes to generate half- and full-scale CBB–LIB models with excellent Li^+ ion diffusions, superior recovery capability rates, high battery energy densities, and high charge/discharge capacities (Scheme 1). Heterogeneous composites were formed along the CBB–anode/–cathode surfaces through the robust coating of the CBB–LFPO cathode and CBB–HS anode geometrics with 1 nm to 5 nm carbon coverage layers (Figs. 1 and 2). The surface heterogeneities, interfaces, and mesh topologies of the CBB–LFPO@C cathode and CBB–HS@C anode geometrics facilitate the electron/Li^+ ion transport and enhance the electric conductivity of CBB–electrodes that are designed in variable half-, full-, and pouch-type LIB model systems (Figs. S4- S12).

Scheme 1

3D multi-functional architectonics with various heterogeneous composites of CBB–LFPO@C cathodes in variable geometrics (e.g., CBB–SE@C, CBB–AB@C, and CBB–CC@C cathodes) and HS@C anode materials were fabricated by using particle-by-particle growth seeds under controlled time, temperature, and composites. The reducing agent power of Fe(III)–anions plays a

key role in controlling low kinetic growth, thermodynamically stable formulation, and exposed surface directions, thereby making these anions crucial in fabricating a 3D CBB–LFPO-hierarchy with variable CBB–SE@C, CBB–AB@C, and CBB–CC@C geometrics (see supporting information S4 to S10).

During the synthesis formulation, the hierarchical deformations in the architectonic orientations facilitated the creation of (i) a cluster of structurally complex 3D CBB–LFPO@C cathode and CBB–HS@C anode materials, (ii) non-energy-consuming surfaces for facile transport systems, and (iii) a long range of space vicinities along the fore- and hind-wings and limbs, nodule- and tip-head/tail, and trial/vein edges for strong-force and long-standing LIB pocket-storage patterns. The electronic conductivity and surface energy of 3D multi-functional CBB architectonics were also improved via the homogeneous and sustainable dressing of the CBB–HS anode and CBB–SE, CBB–AB, and CBB–CC cathodes with the nano-C-wrapped layer (~1 m to 5 nm) along the hierarchical surface models, which can also enhance LIB cyclic stability and facilitate electron/Li^+ ion transport.

Figure 1

Figure 2

High-precision microscopic analyses using FE-SEM (field emission scanning electron microscopy), HR-TEM (high-resolution transmission electron microscopy), ED (electron diffraction), DF- and BF-STEM (dark- and bright-filed scanning transmission electron microscopy), and EDS (energy-dispersive spectroscopy) were carried out to investigate the hierarchical structure of the 3D CBB–architectonics of LFPO@C–cathodes with variable geometric units mimicking SE@C, AB@C hornwracks, CC@C cathode, and HS@C anode surfaces (Figs. 1, 2, S3, and S4). The microscopic patterns (Figs. 1 and 2) show the CBB

anode/cathode electrode architectonics. The CBB-microscopic architectonics indicate the formation of complex uni-, bi-, and tri-modal-hierarchy morphologies, multi-directional configurations, geometrical assemblies oriented in nano-/micro-scale structures, and surface mesh topologies. These CBB–cathode and CBB–anode architectonics enable multi-gate transport and facilitate the continuous flow distribution dynamics of electron/Li^+ ions during multiple lithiation/delithiation processes (>>2,000 cycles). [48-55]

The well-dispersed surface heterogeneity, thermal-stability, and unique configurations and geometrics of CBB–cathode and CBB–anode architectonics were characterized via XRD (X-ray diffraction), TG (thermo-gravimetry), XPS (X-ray photoelectron spectrometry), Raman spectroscopy, N_2 isothermal analyses, and FTIR (Fourier-transform infrared spectroscopy) techniques (Figs. S5 to S10). The crystal structures and geometric properties of the 3D multi-functional architectonics of pure orthorhombic olivine-type structure LFPO@C–cathodes with variable geometric units (e.g., CBB–SE@C, CBB–AB@C, and CBB–CC@C cathode surfaces and ATO CBB–HS@C anode) were characterized via X-ray diffraction (Figs. S10 A and B).[48- 50]

In-/out-plan-view projections of 3D CBB–anode/–cathode electrode surfaces

Figure 3 illustrates the 3D modeling orientations of complex CBB–LFPO@C cathode geometrics and architectonic manifold surfaces along the in-/out-plan-view projections. The projection design supports the formation of multi-diffusion systems onto CBB–anode/–cathode surface faces, edges, vortices, and ridges. Along these topographic complex configurations, window diffusion functions were oriented throughout the entire surface vicinity, circular vorticity, and dimensional dynamics of super-complex CBB–anode/–cathode architectures (Figs. 3A to 3C). The diffusible window functions were precisely associated through the surface meshes, including caves, kinks, vertices,

edges, vortex, holes, bowls, and closely packed capes. The outer-skin CBB–anode/–cathode surfaces with open-window porous entrances, multi-hole vortices, and accessible surface meshes enabled the creation of sustainable, full-scale CBB-mutated-LIBs with continuous and non-resisted surface transports and sensible distribution of electron/Li^+ ions (Figs. 1 and 2).

The structural configurations reveal uniformly oriented CBBs along the anode//cathode surfaces and uniquely featured CBB-mutated-LIB CR2032-circular cells with electrode surface designs (see Figs. 1, 3, S3, and S4). The unique features of CBB–LFPO@C cathode and CBB–HS@C anode materials are summarized as follows:

(i) The interior/exterior CBB–surface interfaces show intrinsic and diverse vicinities, such as in-plane circular swirls, vortex nests, grooves, winglets, protuberances, V-hooks, trails, ridges, caves, and top-pipe-holes upon axially aligned arrays in multiple dimensions (Figs. 1, 3, S3, and S4). The influential power energy density of CBB–LIBs can be ascribed to these surface meshes and space vicinities.

(ii) The external stimuli CBB-engineered surface aligns the anode/cathode assembly with variable geometric CBB–SE@C, CBB–AB@C, and CBB–CC@C cathode blocks and CBB–HS@C anode architectonics. These CBB structures have topographical surface maps, a 3D-dominant orientation, a multi-scale arrangement, and effective complex structures that facilitate the multi-diffusivity, accessibility, and mobility of electron/Li^+ ions. Facile Li^+ ion movements are observed along the critically created spiral/axial/swirl complexities, circular vorticity, and the nests, hornwracks, needles, spherulites, and cube blocks distributed along anode/cathode surface projections (Fig. 3).

(iii) The diverse interior scales of CBBs associated with the variations in open vacancies, vertices, edges, and spaces may modulate a mass of V-caves, ridges, and cage cavities. These free

occupation sites, open-pore systems, and connective open micro/mesoscopic window pores maintain the Li^+ ion diffusion efficiency during charge/discharge processes and facilitate the electron/Li^+ ion transfer at the electrolyte/CBB–solid electrode interfaces.

(iv) The overall CBB–cathode/–anode configurations and geometrics manipulate the complexity of vortices, uni-, bi-, and tri-modal-hierarchy morphologies, multi-directional configurations, and geometrical assemblies. These CBB architectonics act as the driving forces behind the modulation of the continuous, wide-ranging Li^+ ion flow distribution dynamics along in-/out-plane circular swirls running over the inner/exterior vicinities and cavities of CBB–cathode/–anode surfaces.

(v) The stimulus dynamic transport-gates and windows along the designed CBB-mutated-LIBs reached their maximum discharge rate capacities during the innumerable lithiation/delithiation (discharge/charge) cycling processes (>>2,000 cycles) of CBB–LIBs (Fig. 3).

Figure 3

Configured geometrics of variable CBB-mutated-LIB CR2032-circular coin models

The integration of 3D CBB-anode/-cathode electrode architectonics enables the fabrication of diverse scales of LIB pattern assemblies. For instance, we aligned variable CBB–LFPO@C cathode half-cell LIB geometric blocks, including SE@C–, AB@C–, and CC@C–cathodes. We also formulated CBB–anode half-cell LIB designs with CBB–HS@C geometrics. Full-cell CBB–LIB CR2032-circular coin designs were fabricated with effective CBB–SE@C cathode//CBB–HS@C anode configurations. As the driving forces behind the modulation of large-scale CBB-pouch-type LIBs, compact anode/cathode CBB-mutated-LIB CR2032-circular coins were packed tightly in series by following a dense collar packing protocol. In all designed CBB-mutated-LIB

models, the effects of modulated key structures, such as complex uni-, bi-, and tri-modal-hierarchy morphologies, multi-directional configurations, geometrical assemblies, and surface mesh topologies, on the influential power tendency of CBB-mutated-LIBs were intensively investigated (Figs. 4- 6, S11, and S12).

Variable CBB-LFPO@C (CBB-P cathode) half-cell LIB geometric models

To study the effect of the CBB architectonic configurations and geometrics in LIB models, we aligned variable 3D CBB–LFPO@C cathodes, including CBB–CC@C, CBB–AB@C, and CBB–SE@C geometrics, on half-cell LIB CBB–P CR2032-circular coin designs (Figs. 4, 5). The CV sets of CBB–SE@C–, CBB–AB@C–, and CBB–CC@C–P cathode LIBs were designed at 0.1 C and a potential window range (2.0 to 4.3 V), as seen in Figure 4(a). The significant changes in the oxidation (delithiation)/reduction (lithiation) Fe^{2+}/ Fe^{3+} ($LiFePO_4$/$FePO_4$) profiles for CBB–P cathode LIBs were obtained at potentials of 3.33/3.5 V (CBB–SE@C), 3.28/3.59 V (CBB–AB@C), and 3.18/3.67 V (CBB–CC@C).[53,54] Figure 4b shows the influence of the CV profile CBB–SE@C–cathode LIB–CR2032 design sets at C-rates (0.1C to 5C) and potential ranges (2.0 V to 4.3 V). Increasing the scan-rates leads to enhance and reduce the V of both oxidized and reduced peaks, respectively, and enriches their current (mA). The CBB–SE@C–cathode LIB–CR2032 design cycling performances (i.e., during the 1^{st} to 500^{th} cycles) were examined at potential ranges (2.0 V to 4.3 V), see Figure 4c. The symmetrical peaks of representative anode-oxidation/cathode-reduction Fe^{2+}/ Fe^{3+} ($LiFePO_4$/$FePO_4$) formulations were observed at 3.28/3.56 V with an average operating voltage of 3.45 V. The symmetrical behaviors in these oxidation/reduction peak profiles indicate highly reversible levels of delithiation/lithiation reactions even after 500 cycles. [51, 52]

Figure 4

Figures 4d-g illustrate the key geometric influence of 3D CBB–LFPO@C CBB–P cathode electrodes, including CBB–SE@C, CBB–AB@C, and CBB–CC@C structural designs, on the stability of CBB–P cathode half-cell LIB-CR2032 circular designs. The stability of CBB–P cathodes was determined as a function of specific discharge capacity, non-resistance electron/Li+ ion surface spreading and transport, electrical conductivity, and rate capability (Figs. 4d to 4g, respectively). As a systematic model of hierarchical CBB–P complexity, we also examined the influence of CBB–LFPO@C geometrics on the reversibility and stability of the capability rates of CBB–P cathode half-cell-LIB CR2032 circular designs. The reversibility and capability rates of half-cell CBB–LFPO@C cathode LIB CR2032-circular coin models were also inspected at various C-rates (0.1 C to 20 C), cycle numbers (1 to 100 cycles), and voltages (2.0 V to 4.3 V) at a fixed temperature of 25 °C (Fig. 4d). The specific discharge capacity ($mAhg^{-1}$) for all half-cell CBB–SE@C, CBB–AB@C, and CBB–CC@C cathode LIB geometric models was investigated at C-rates (0.1, 0.2, 0.5, 1, 2, and 5 C), while maintaining 10 cycles at each C-rate (i.e., 1st to 60th cycles) (Fig. 4d). The discharge capacity for all half-cell CBB–SE@C, CBB–AB@C, and CBB–CC@C cathode LIB geometric models decreased along with increasing C-rates and cycle numbers. We also examined the lithiation/delithiation reversibility of the discharge capacity sets under irregularly changing C-rates and high cycling numbers (60 to 100 cycles). The stimulus discharge capacity that was continuously recorded from 0.1 C to 5 C and up to 60 cycles moves back to C-rate at 0.1C and then transfers to 10 C as the number of cycles varied between 60 and 80. To highlight the unique reversibility of rate capability at 80 to 100 cycles, the discharge capacity pattern (recorded at 1 C and 5 C and at 40 and 60 cycles) went back to both C-rates (1 C and 20 C) at the 90th and 100th cycles, respectively. The recovery of rate capability profiles at various C-rates for all half-cell CBB-cathode LIB models demonstrates the sustainable reversibility of

delithiation (i.e., Li^+ ion segregation)/lithiation (i.e., Li^+ ion intercalation) processes even at the 100th cycle.[55]

We also examined the stability of the 1st specific discharging capacity of CBB-cathode-half-cell LIBs versus multiple cycle numbers (1 to 100) at 0.1 C (Fig. 4e). The CBB–SE@C, CBB–AB@C, and CBB–CC@C electrodes on the half-cell CBB–cathode LIB CR2032-circular coin designs achieved specific discharge capacities of 92.5%, 86.7%, and 81.5% after 100 cycles, respectively. The lower capacity decline of CBB–SE@C half-cell cathode LIBs compared with CBB–AB@C and CBB–CC@C geometric cathodes suggests the long-term lithiation/delithiation reversibility. Therefore, the prominent CBB–SE@C hierarchy models provide additional leverage to ensure that CBB–SE@C half-cell cathode LIBs have an excellent electrochemical quality.

The key value of CBB–LFPO@C architectonic, configuration, and geometric cathodes in leveraging the non-resistance electrode capability of half-cell CBB–P cathode LIB CR2032-circular coin models was then examined by performing electrochemical impedance spectroscopy (EIS) measurements and by referring to the equivalent circuit (Fig. 4f, inset). [48-55] The EIS parameters for CBB–LFPO@C geometric cathodes are provided in Table S1. [5,13] The obtained Nyquist-semicircles graphs and the equivalent charge transfer resistance (R_{ct}) of variable 3D CBB–LFPO@C cathode electrodes, including CBB–SE@C, CBB–AB@C, and CBB–CC@C geometrics, indicate the leverage of the functional surface mobility of CBB-cathode geometrics. Among all half-cell CBB–P cathode LIB CR2032-circular coin models, the 3D CBB–SE@C cathode electrode surface has smallest semicircle diameter and lowest R_{ct} value (~74Ω), thereby indicating that the electrode surfaces have a high exchange current density (i_0). Therefore, among all available electrodes, the CBB–SE@C–cathode electrode has the fastest transport mobility, best diffusion kinetics, lowest resistance, and shortest transport path for electrons/Li^+ ion movements.

The CBB–SE@C–cathode LIB model also shows excellent electrochemical performance and cycle reliability due to its critical 3D hierarchical super-scale CBB–SE@C architectonics cathode features with uni-, bi-, and tri-modal- geometrics, exposed multi-surface facets, axial dimensions/directions, large V-angular vacancies surface mesh topologies, coral channel through pipes, and linear needle canals (see Fig. 3). [22, 50, 51]

The effects of CBB–LFPO@C geometric cathodes on the stimulus sustainability of half-cell CBB–P cathode LIB models were then investigated at varied temperature ranges (Fig. 4g). The sustainability of a half-cell CBB-cathode LIB battery was also assessed in terms of its perspective conductivity and electronic mobility at high temperatures (~250 K to 455 K). The electrical conductivity for all CBB–LFPO@C architectonic configurations and geometrics gradually increased along with temperature. The conductivity of the half-cell CBB–SE@C cathode LIB differed from that of other CBB–P cathodic CBB–AB@C and CBB–CC@C models over a wide temperature range (i.e., ~250 K to 455 K). The excellent battery sustainability of half-cell CBB–LFPO@C cathode LIBs highlights the value of hierarchical CBB structure models. For instance, the CBB–SE@C cathode electrode shows that highly stable surface mesh topologies can maintain transport mobility and strengthen the maximum driven-force modulation in electron/Li+ ion movements under highly thermal conditions.

Figure 5

The influence of the specific CBB architectonics of 3D CBB–LFPO@C configurations, geometrical assemblies, and surface topologies on the charge–discharge cycling profiles of half-cell CBB–cathode LIB CR2032-circular coin designs was then explored, as shown in Figure 5. The first-cycle discharge capacity performance was gradually reduced by the elevation of C-rates of CBB–SE@C, CBB–AB@C, and CBB–CC@C half-cell CBB–P cathode LIB models (Fig. 5a).

At all C-rates, the first-cycle specific capacity performance of CBB–P cathode half-cell-LIB CR2032-circular coin designs was reduced in the following sequence: CBB–SE@C > CBB–AB@C > CBB–CC@C cathode LIBs. Fig. 5b shows the effect of variable 3D CBB–LFPO@C geometrics on the first-cycle lithiation/delithiation process of half-cell CBB–SE@C, CBB–AB@C, and CBB–CC@C cathode LIBs at a voltage range (2.0 V to 4.3 V) and at C-rate (0.1C) (Fig. 5(b)). The CBB–SE@C P–cathode shows a higher lithiation/delithiation storage capacity compared with the geometrics of CBB–AB@C and CBB–CC@C designed in half-cell cathode LIBs. In addition, the half-cell CBB–SE@C, CBB–AB@C, and CBB–CC@C cathode LIBs obtained 1^{st} specific discharging capacities (167.4, 155, and 142.9 $mAhg^{-1}$, respectively), at 0.1 C. We also examined the effect of various C-rates (0.1 C to 20 C) and lithiation/delithiation cycles (1 to 100 cycles) on (i) the 1^{st} specific discharging capacity and (ii) stable behavior of the charge/discharge (lithiation/delithiation) process of half-cell CBB–SE@C cathode LIBs, as seen in Figs. 5c and 5d, respectively. The charge/discharge profiles show that the first-cycle discharge capacity of CBB–SE@C electrode geometrics remains stable at C-rates of 0.1 C to 20 C and at 1^{st} - 100^{th} cycling processes. Therefore, the cycling numbers and discharge capacities of the charging/discharging profiles of the CBB–SE@C–cathode LIB–CR2032 design differ from those of other half-cell CBB–LFPO@C LIB configurations.

The above findings also highlight the stable behavior of the discharge capacity pattern at low/high C-rates and varying cycle numbers (Fig. 4d). For instance, the discharge capacity recovered along with a changing C-rate (i.e., from 0.5 C to 0.1 C and from 10 C to 1 C). These results highlight the excellent lithiation/delithiation reversibility and rate capability of half-cell CBB–LFPO@C cathode LIB models. The CBB–SE@C, CBB–AB@C, and CBB–CC@C electrodes designed in

the half-cell LIBs retained 121.0, 51.8, and 19.5 $mAhg^{-1}$ of their initial discharge capacities (Figs. 5b and 5c) at 20 C and at the 100th cycle, respectively. These electrochemical measurements and the diverse performance scales of half-cell CBB–cathode LIB CR2032-circular coin designs suggest that CBB–SE@C and the cathode geometric electrode serve as extraordinary models of hierarchical CBB-mutated-LIBs. The outstanding stable behavior of the CBB–SE@C cathode is a key function of novel LIB models that may satisfy the sustainable energy density requirements of EVs. The uni-, bi-, and tri-modal-architectonic morphologies and vacant surface mesh topologies of the CBB–SE@C cathode electrode also play important roles in improving the sustainability of Li^+ ion diffusions, the rate of recovery capability, energy density, and charge/discharge capacity of hierarchical CBB-mutated-LIBs (Figs. 4, 5).

CBB–HS@C anode half-cell LIB CR2032-circular coin design

As complex hierarchical structures, CBB–HS@C anode geometrics with morphological reef-ball spherulites, interior/exterior space surface meshes, and vortex cavities affect the potential anode electrode in the integral half-cell anode LIB CR2032-circular coin design (Figs. S11 and S12). The multi-directional configurations and geometrical assemblies of CBB–HS@C materials play important anode electrode functions that can promote high flow dynamics and Li^+ ion host-open accommodation pockets.

The charge/discharge profile sets of half-scale CBB-HS@C anode LIB CR2032-circular coin designs were recorded at C-rates (0.2 C to 20) and at voltages (1.0 V to 3.0 V) (Fig. S11a). The reduction in discharging capacity profile (i.e., from 3.0 V to 1.7 V) was indicated the behavior of the lithiation process (i.e., Li^+ ion intercalation) along the CBB–HS@C anode electrode. The superior recovery of Li^+ ion intercalation at all C-rates reduced the specific capacity at 1.0 V. However, the charging/delithiation (i.e., Li^+ ion segregation) processes increased the potential

from 1.0 V to 1.9 V at all C-rates. The sharp increase in the charging profile of the CBB–HS@C anode electrode indicates the massive loading of the Li^+ ion into the vortex cavity during the delithiation process. Figure S11b shows the discharging capacity of the half-scale LIB based on CBB–HS@C anode electrode during the first cycle, which is gradually reduced along with an increasing C-rate. At 20 C, the 1st specific discharging capacity performance of the CBB–HS@C anode electrode reached 88.7 $mAhg^{-1}$ at 0.2 C. The Nyquist study of the CBB–HS@C anode half-cell LIBs revealed the semicircles as a result of the electron/Li^+ ion-transport mobility along anode electrode surface. The equivalent R_{ct} indicates that CBB–HS@C anode geometrics have passable electrons/Li^+ ion dynamics and diffusions along the spiral/axial/swirl directions, in-plane circular vortices, and the entire reef ball nests of anode surfaces (Fig. S11c).[55]

The effects of CBB-engineered HS@C anode configurations on the long-range cycling, good stability and capability behaviors of the half-cell CBB–HS@ anode LIBs were investigated at various C-rates (0.1 C to 20 C), cycle numbers (1 to 100), and voltages (1.0 V to 3.0 V) at a fixed temperature of 25 °C (Fig. S12). The experimental sets underscore the highly reversible rate capability of the half-cell CBB–HS@C anode LIB CR2032-circular coin design. The rate capability pattern recorded at 20 C and the 100th cycle reveals that the CBB–HS@C anode electrode retains 89.2 $mAhg^{-1}$ of its initial discharge capacity. The distinct capability rate and stability performances of specific discharging/charging capacities may indicate the important function of the CBB–HS@C anode electrode with 100 nm multi-holes along its spherulites-like reef ball vortices and intrinsically ordered 1 nm to 3 nm carbon layers (Figs. 2A to 2E). Meanwhile, the CBB–HS@C surface mesh topologies indicate the formation of free-occupation meso-cages and highly diffusible entrance windows and voids along the anode surfaces, which can facilitate the Li-ion movability and diffusivity kinetics during lithiation/delithiation processes (Fig. 3).

Full-cell CBBs-mutated-LIB CR2032-circular coin design

As systematic hierarchical anode//cathode complex models, we chose the CBB–HS@C anode (N)//CBB–SE@C cathode geometrics as distinct CBB-N//-P electrodes for designing full-scale CBB-mutated-LIB CR2032-circular coin cells (Fig. S1). The occupant mass loading and rational capacity balancing ratio (i.e., CBB-N//-P)$_{Cap}$) are key factors in fabricating safe CBB-mutated-LIB cells and maintaining their high battery energy density. To reduce the influence of highly doped Li^+ ion layers that are formed on CBB electrode–film surfaces as a result of the excellent reversibility of the entire charge/delithiation and discharge/lithiation processes, we tested a control over (CBB-N//-P)$_{Cap}$ mass balancing. Our experiments show that the (CBB-N//-P)$_{Cap}$ mass balancing with 1.09:1.0 ratio leverages the production of high specific energy density battery for the designed full-scale CBB-HS@C anode (N) // CBB-SE@C cathode (P) CBB-mutated-LIB CR2032-circular coin cells. Based on the (CBB-N//-P)$_{Cap}$ ratio control, the specific discharging capacity values of a half-cell LIB CR2032-circular coin cell based CBB–SE@C cathode electrode are 165 and 155.2 mAh/g (Fig. 5c), whereas those for a full-scale CBB-mutated-LIBs CR2032-circular coin cell are 163.6 and 161.3 mAh/g (Fig. 6a) at C-rates (0.1 C and 1 C, respectively).

The electrochemical charging/discharging and C-rate-dependent profiles on the 1st specific discharging capacity performance of full-scale CBB-mutated-LIB CR2032-circular coin-cells designed by CBB–HS@C anode (N)//CBB–SE@C cathode (P) electrodes were tested at potential range (0.8 V to 3.5 V) (Figs. 6a and 6b). The first-cycle specific capacity of CBB–HS@C//CBB–SE@C full-scale CBB-mutated-LIBs gradually reduced along with increasing C-rates (i.e., from 163.6 mAhg^{-1} (at 0.1 C) to 131.7 mAhg^{-1} (at 20 C)). Figure 6a exhibits that the designed full-cell CBB-mutated-LIB has average operation voltage of 1.91 V. Therefore, the CBB structural features

enable the engineering of full-cell CBB-mutated-LIB models with an excellent battery energy density of 154.4 Wh/kg (see supporting information S1). [49-55]

The reversibility and capability rate of full-scale CBB–HS@C anode (N)//CBB–SE@C cathode (P) CBB-mutated-LIB CR2032-circular designs versus C-rates (0.1 C to 20C) and cycle number (1 to 100 cycles) were investigated (Figs. 6c and 6d). The discharge capacity sets ($mAhg^{-1}$) for all full-cell CBB-mutated-LIB models were examined at a C-rate sequence pattern of 0.1, 0.2, 0.5, 1, 2, and 5 C, with 10 cycles per C-rate (i.e., 1 to 60 cycles) (Figs. 6c and 6d). To check the perfect recovery of the reversible lithiation/delithiation process at high cycle numbers, the discharge capacity sets patterned at 1 C and 5 C (i.e., after 40 and 60 cycles, respectively) turned back to those patterned at 1 C and 20 C (i.e., after 90 and 100 cycles, respectively). This finding indicates that full-cell CBB-mutated-LIB models retained 99.9%, 99.1%, 98.7%, and 98.5% of their initial discharge capacity performance. The stable behavior of the discharge capacity patterns underscores the leveraging effects of CBB–HS@C anode (N)//CBB-SE@C cathode (P) architectonics, structural configurations, geometrics, and surface mesh topologies. In sum, the full-cell CBB-mutated-LIB designs exhibit highly reversible lithiation/delithiation and remarkable rate capability performance.

The exceptional stability of full-scale CBB–HS@C anode (N)//CBB–SE@C cathode (P) versus discharge–charge capacity and Coulombic efficacy plays a key role in effectively designing CBB-mutated-LIB CR2032-circular models (Figs. 6e and 6f). The full-scale CBB-mutated-LIB cells retained 81.8% of their initial capacity (i.e., 163.6 $mAhg^{-1}$) and demonstrated a high Coulombic efficacy of approximately ~99.7% at 0.1 C after 2000 cycles. Figure 6f shows that the Coulombic efficacy of this full cell increases from 92% during the first cycle to >99.5% after 40 cycles.

Approximately 100% of this Coulombic efficacy was retained after 2000 cycles. Therefore, CBB–anode/–cathode geometric electrodes provide a configuration of full-scale CBB-mutated-LIBs with high a Coulombic efficacy of ~100%, non-resisted surface mobility, sensible distribution of electron/Li^+ ions, and innumerable lithiation/delithiation (discharge/charge) cycling processes (>>2,000 cycles). Moreover, the architectonic configurations and geometrics of anode/cathode electrodes that modulate full-cell CBB-mutated-LIB CR2032-circular designs are important in enhancing the long-term sustainability, discharge capacity, battery energy density, and Coulombic efficacy of LIBs (see supporting information S13).[1,5-10]

Hierarchical complex CBB-pouch-type LIB cell battery models

We develop compact design-scales of CBB-pouch-type LIBs by using a dense collar packing protocol (Fig. S2). A rational control over well-packing and number of stacked layers and sides, dimensions, and mass component of CBB-HS@C anode (N) and CBB-SE@C cathode (P) electrodes is attested to synthesis CBB-pouch-LIB types. Exemplary CBB-pouch-type models were developed to achieve high cell battery energy density (i.e. gravimetric/volumetric performances), areal capacity, and LIB sustainability. A set of full-cell CBB–HS@C anode//CBB–SE@C cathode CBB-mutated LIBs is often continuously attached and stacked in layers. For instance, the CBB–HS@C anode and CBB–SE@C cathode are designed with 5 and 6 layers, with each layer having 10 sides, in the orientation of the CBB-LIB pouch-model. Accordingly, the configuration sets of the CBB- LIB pouch-type model at 0.1 C achieve excellent gravimetric and volumetric cell specific capacitances (163.6 Ah/kg and 212.47 Ah/L) and cell energy densities (154.4 Wh/kg and 200.5 Wh/L) (see supporting S1 and S3).

In the configuration set of the CBB-pouch-type LIB cell, the large free-space surface area and the mass component of the CBB–HS@C anode (N-electrode)//CBB–SE@C cathode (P-electrode)

should be controlled. The CBB-pouch-type LIB cell is configured at specific 3D cell dimensions (5.5 cm (length), 3.5 cm (width), and ~0.25 cm to 0.3 cm (thickness)). These surface-controlled parameters could help achieve areal discharge capacities of 1.124 mAh/cm^2 and 2.48 mAh/cm^2 for CBB–HS@C anode (N-electrode)//CBB–SE@C cathode (P-electrode) CBB–LIB-pouch configurations at C-rate (0.1 C), respectively. Moreover, the areal energy densities of both CBB–HS@C anode (CBB–N) and CBB–SE@C cathode (CBB–P) electrodes in the configured CBB-pouch-type LIB cell were 2.08 mWh/cm^2 and 4.45 mWh/cm^2, respectively. Controlling the (CBB-N//-P)$_{Cap}$ ratio of active CBB–anode/–cathode materials during the fabrication of N- and P-working electrodes is important in formulating CBB-mutated-LIB CR2032 circular-type and CBB-pouch-type cells.

Conclusion

We present scalable designs of CBB-mutated anode/cathode electrodes and their modulations in diverse scales of half- and full-cell CBB-LIB CR2032-circular coin models. CBB anode/cathode electrode architectonics with complex uni-, bi-, and tri-modal-hierarchy morphologies, multi-directional configurations, geometrical assemblies oriented in nano-/micro-scale structures, and surface mesh topologies were also built along with a large number of bristles, corrugations, and tercets that are woven into tightly folded winglets to facilitate the development of half- and full-cell CBB-LIB CR2032-circular coin designs. The CBB-mutated-LIB CR2032-circular designs exhibit the maximum possible specific discharging capacity of 163.6 mAh/g (at 0.8 V–3.5 V and at 0.1 C), high Coulombic efficacy (~99.7%), durable rate capability, and reversible diffusion systems after multiple lithiation/delithiation (discharging/charging) cycles (i.e., >>2,000 cycles). The full CBB–LIB pouch models also have a high battery energy density of 154.4 Wh/kg. We

develop compact CBB-pouch-type LIBs by following a dense collar packing protocol, in which a set of anode/cathode electrodes designed in CBB-mutated-LIB pouch-type LIBs are continuously attached and stacked in layers. A rational control over N/P balancing ratios, number of stacked layers and sides, and dimensions during the design of CBB-LIB pouch configurations can lead to the excellent cell battery energy density (i.e., gravimetric/volumetric performances), areal capacity, and sustainability of LIBs. The CBB-pouch-type LIB models that comprise multiple uni-, bi-, and tri-modal architectonics can benefit the LIB technology by offering a sustainable electron/Li^+ ion storage, a stable diffusion and accommodation capacity, and an excellent retention of high specific energy density, all of which can fulfill the powerful force-driving range and tradeoff requirements in EV applications.

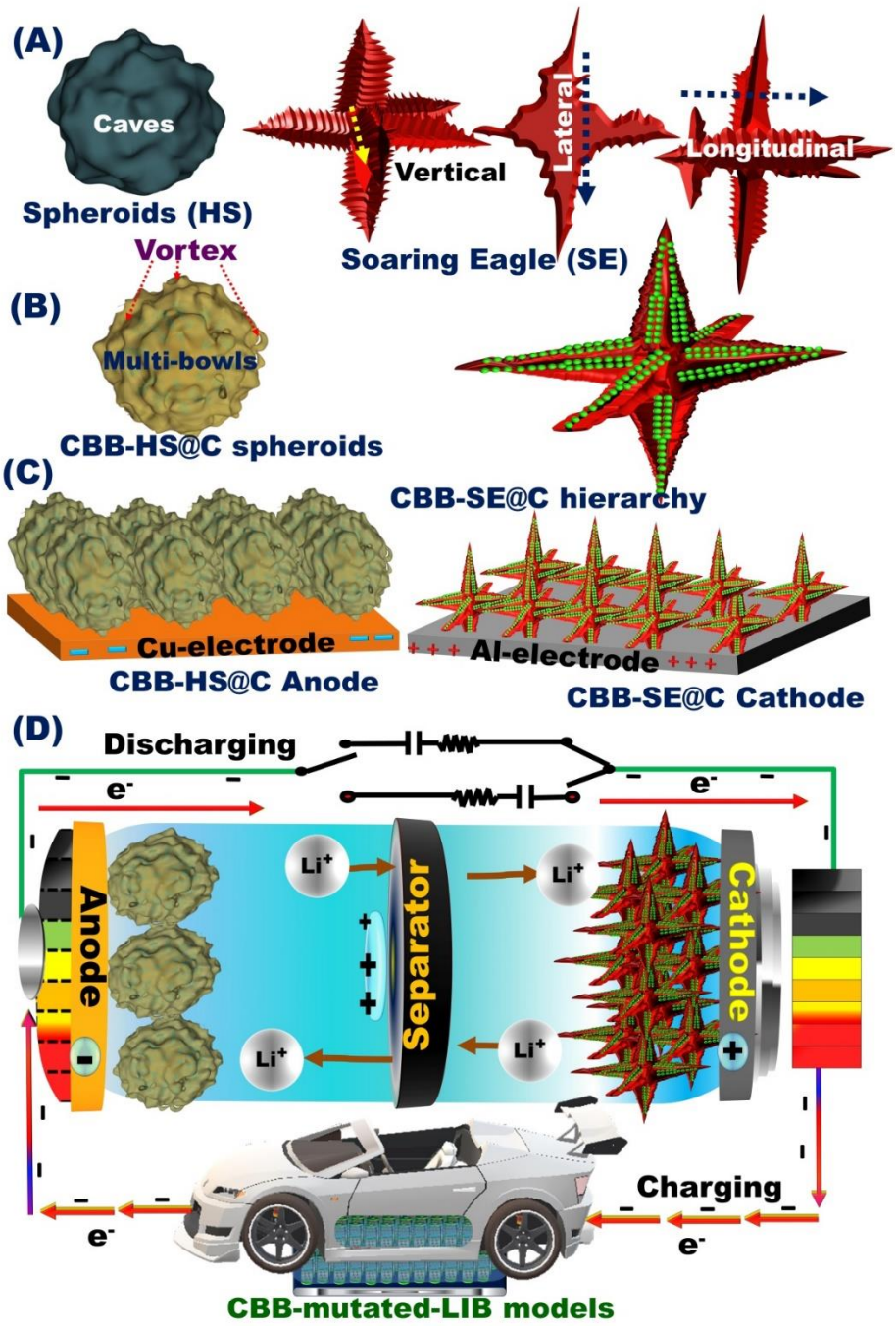

Scheme 1 (A-B) 3D projection models and hierarchical structure directions in variable uni-, bi-, and tri-modal-hierarchies of CBB-LFPO and CBB-LFPO@C cathode and CBB-HS and CBB-HS@C anode materials. (C) Fabrication of CBB-P and CBB-N electrodes into Al-foil (10 µm-thickness) and Cu-foil (8 µm-thickness), and films. (D) Full-scale CBB-HS@C anode (N) // CBB-SE@C cathode (P) CBB-mutated-LIB models and the mechanistic Li^+ ion-rechargeable battery during the electron/Li^+ ion movement and diffusion within lithiation/delithiation (i.e., discharging/charging) process.

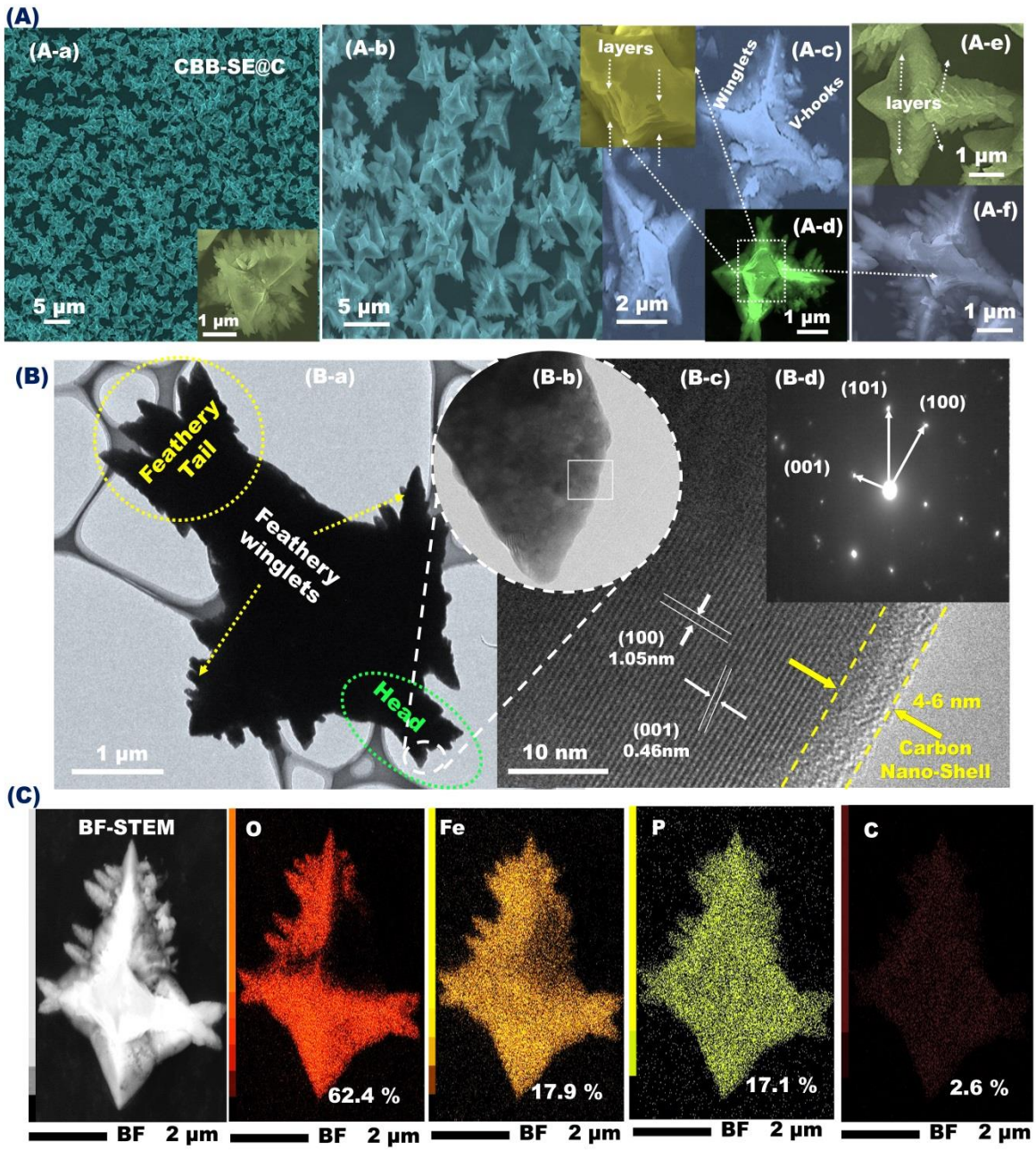

Figure 1 (A-C) FE-SEM (A-a and A-f), HR-TEM (B-a to B-c), ED (B-d), and BF-STEM and EDS (C) microscopic patterns of CBB-LFPO@C geometric units with CBB-SE@C architectures. **(C)** The BF-STEM-EDS mapping of the elements distribution in the CBB-SE@C materials indicated the presence of O: Fe: P: C with ratio of 62.4%:17.9%:17.1%:2.6%, respectively. (B-d) ED image analyzed on [010] crystallographic direction of CBB-SE@C cathode geometrics.

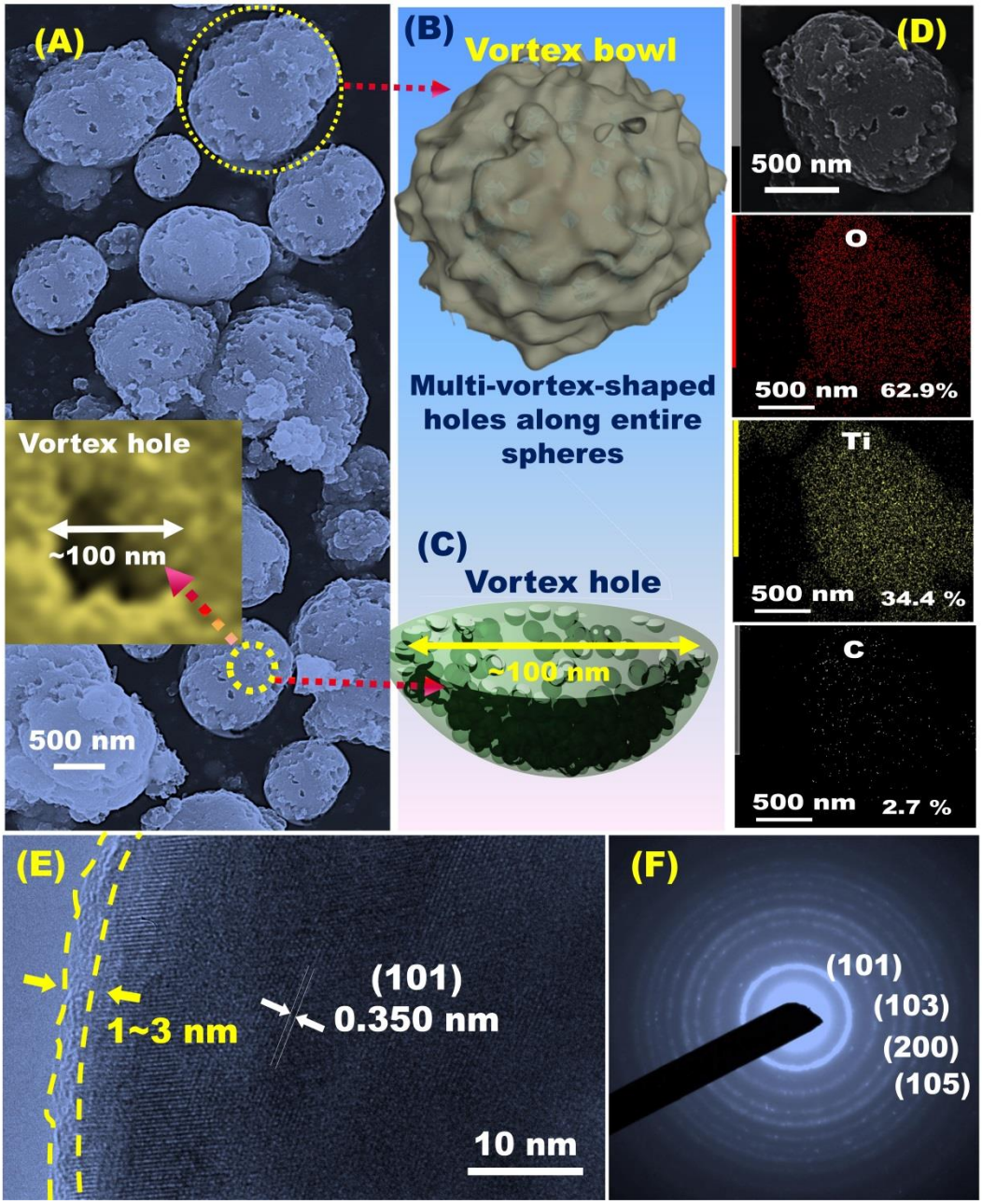

Figure 2 FE-SEM (A), exterior surface design (B), interior vortex shape (C), DF-STEM and EDS (D), HR-TEM (E)), and ED (F) microscopic patterns of anatase TiO_2@C multi-hole spherulites-like reef ball vortices (HS@C anode). **(D)** The mapping of the elements distribution in the CBB-HS@C material indicated the presence of O: Ti: C with ratio of 62.9%: 34.4%: 2.7%, respectively. (E) HR-TEM micrographs of the outer edge entrance of the vortex-shaped bowl of CBB-HS@C geometrics, showing the 1-3 nm-ridges along the circular ripple of the exterior edge of core holes. (F) ED image analyzed on [101] plane of CBB-HS@C anode geometrics.

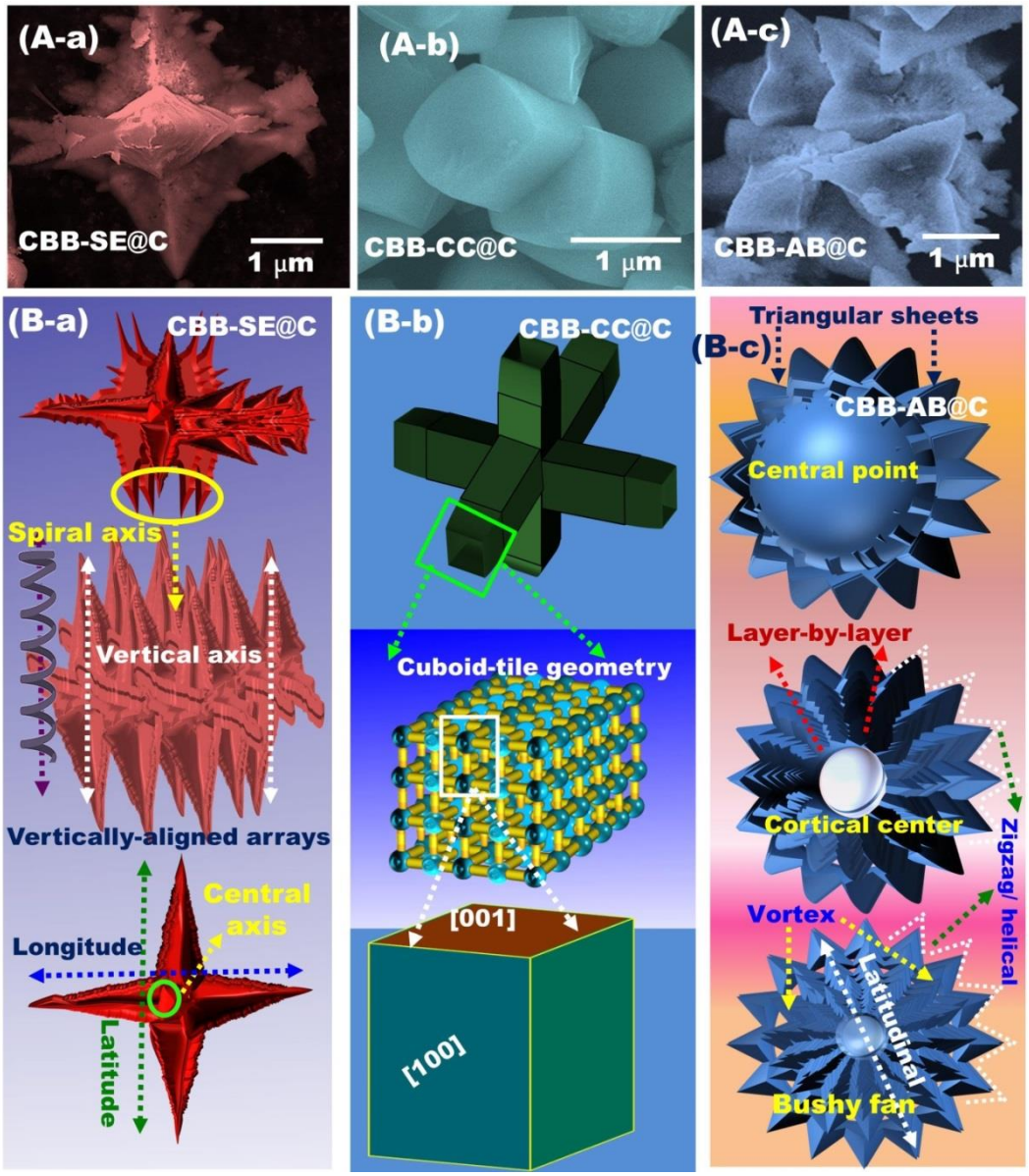

Figure 3 (A-a-c) Microscopic structures based SEM patterns and (B-a-c) 3D modeling objects of CBB cathode materials designed with morphologically-shaped complex configurations, multi-directional and uni-, bi-, and tri-modal orientations, geometrical assemblies oriented in nano-/micro-scale structures, and diverse surface topologies. The systematic representation of 3D CBB-objects and mesh-surface-projections of in-plane axial and central axes, vortex nests, grooves, winglets, protuberances, V-hooks, trails, ridges and caves, and top-pipe-holes upon axially-aligned arrays in multi-dimensions.

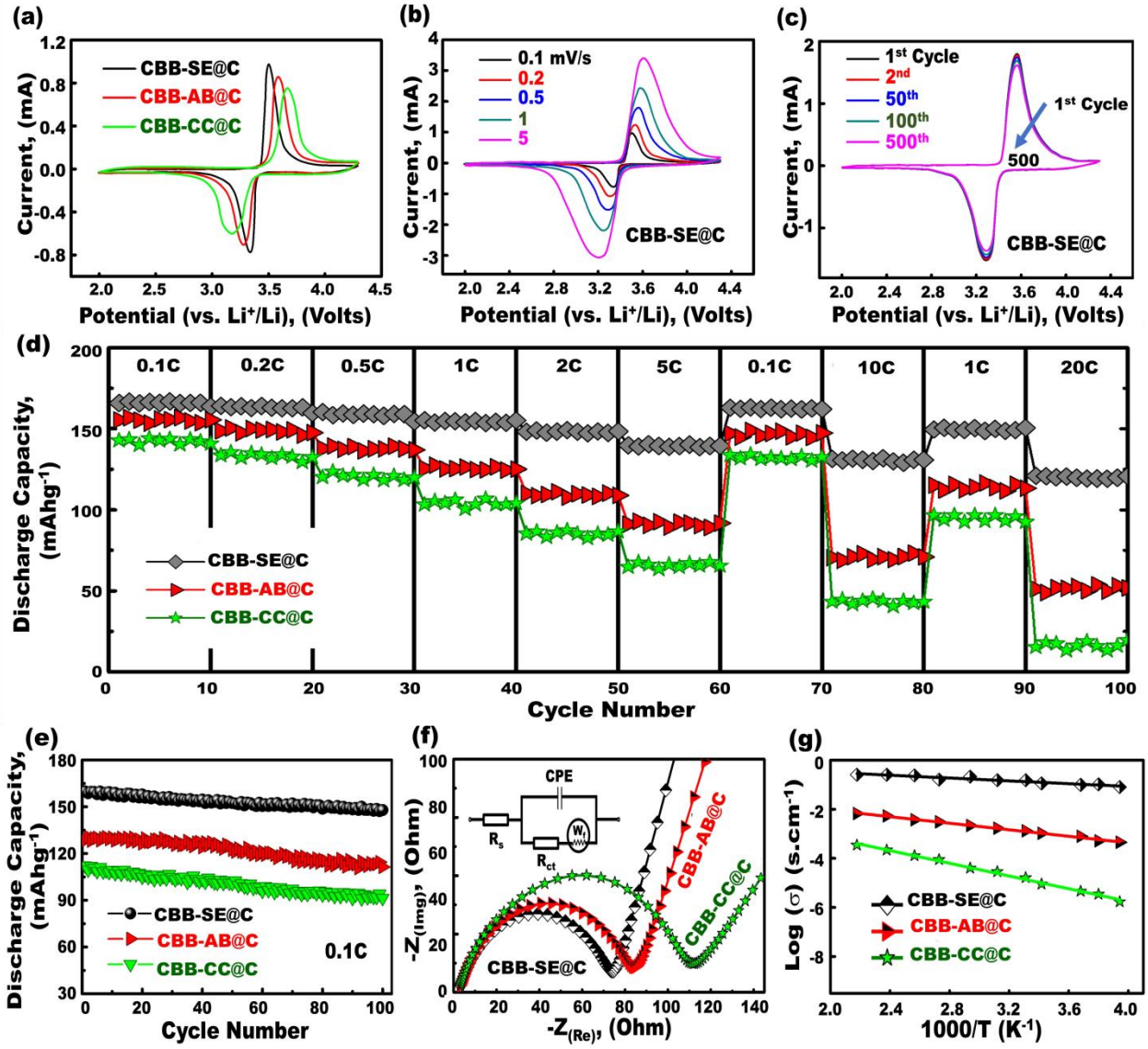

Figure 4 (a, b and c) CV (cyclic voltammogram) profiles of variable 3D CBB-LFPO@C cathodes, including CBB-SE@C, -AB@C, and -CC@C geometrics, on half-cell CBB-cathode LIB CR2032-circular coin designs. CV measurements are studied as a function of CBB-LFPO@C geometrics (a), different sweep rate (b), and cycle numbers (1^{st} -500^{th} cycle ranges) (c). (d-g) Functional stability of the electrochemical performances of variable 3D CBB-LFPO@C cathode electrodes, including CBB-SE@C, -AB@C, and -CC@C geometrics that fabricated the half-cell CBB-cathode LIB CR2032-circular coin designs in terms of capability performance rate (d), specific discharge capacity (e), non-resistance electron/Li+ ion surface spreading and transport (f) and electrical conductivity (g). Note: the measurement sets are as follows; (d) rate capability performance at multiple cycling (e) cycling performance stability, (f) the electrochemical impedance spectroscopy (EIS), (g) temperature-dependent (at ~ 250 to 455K ranges) electrical conductivity.

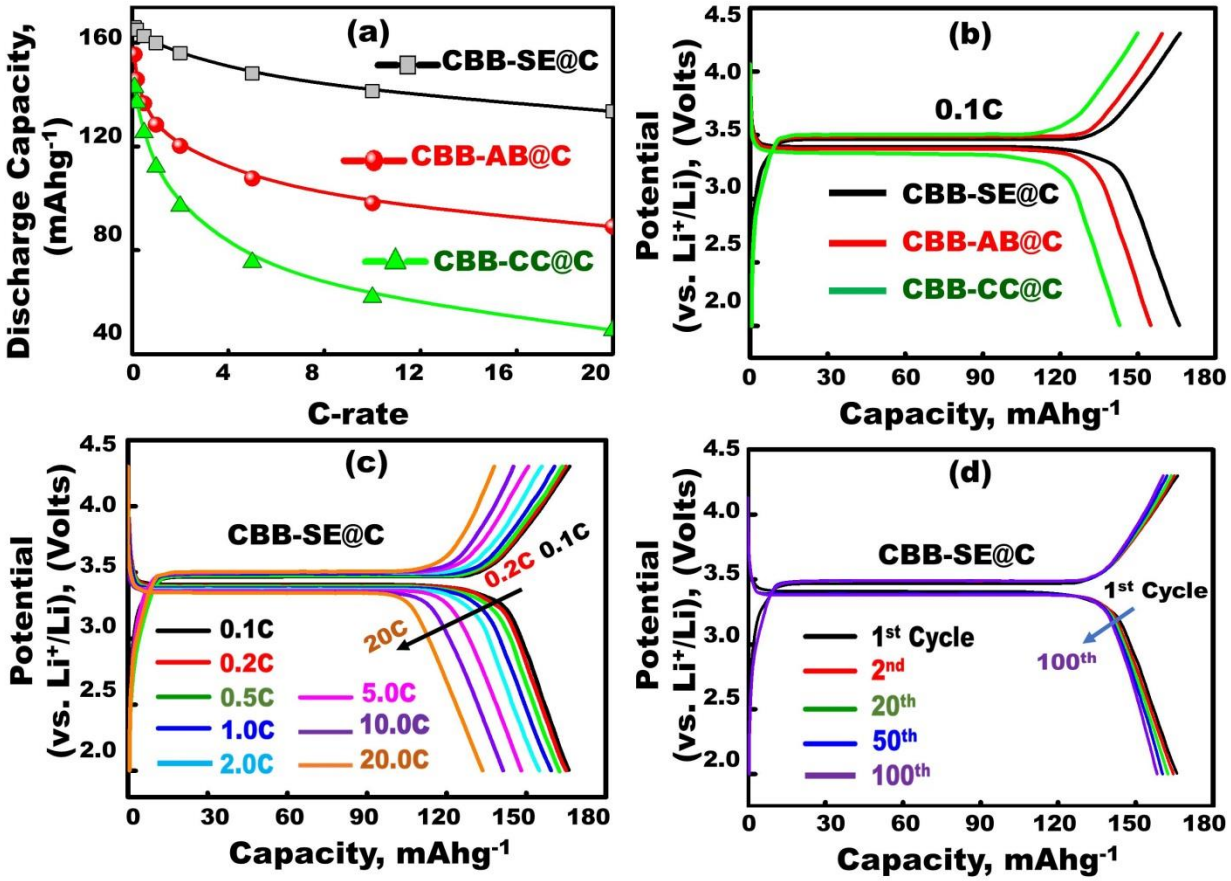

Figure 5 (a-d) Study the performance and effect of 3D CBB-LFPO@C configurations including (CBB-SE@C, -AB@C, and -CC@C) cathode geometric electrodes on the fabricated half-cell CBB-cathode LIB CR2032-circular coin designs as a function of 1st cycle discharge capacity (a), charge–discharge capacity (b), various C-rate (0.1C-20C) ranges (c), and a number of lithiation/delithiation cycling (1st-100th cycles) processes (d).

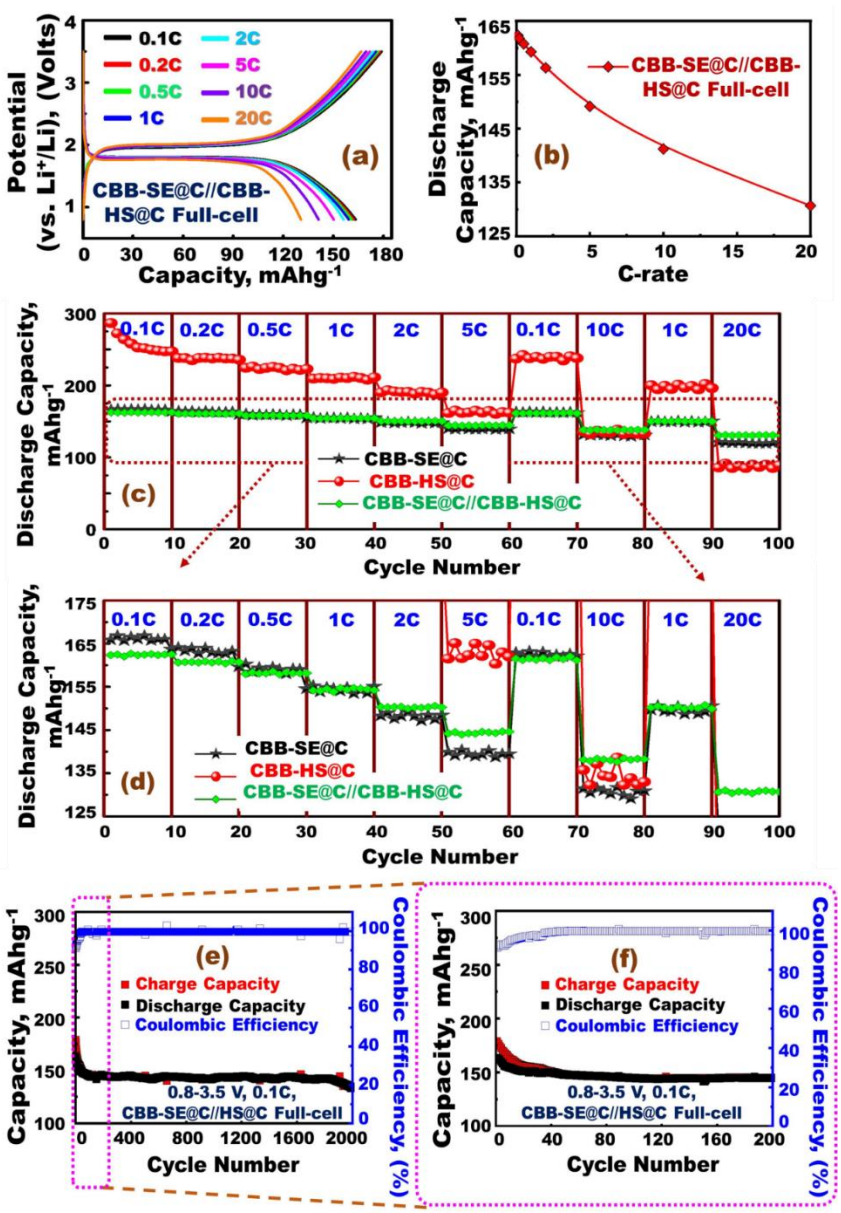

Figure 6 (a-f) The electrochemical performances of full-scale CBB-HS@C anode (N) // CBB-SE@C cathode (P) CBB-mutated-LIB CR2032-circular coin cells in terms of charge-discharge plot (at different C-rates) (a), specific discharging capacity (at different C-rates) (b), capability performance (c,d), and charge- discharge capacity and Coulombic performance efficacy sets (e,f). Note: the measurement sets are as follows, (a,b) C-rate-dependent profile of 1st specific discharging capacity, (c, d) the reversibility and rate capability performances, (e,f) the stability of discharge-charge capacity and Coulombic performance efficiency, respectively. (d and f) Enlargement plots (d and f) are represented the electrochemical measurements (c and e), respectively.

REFERENCES

(1) Saravanan, K.; Ananthanarayanan, K.; Balaya, P. Mesoporous TiO_2 with high packing density for superior lithium storage. *Energy Environ. Sci.* **2010**, *3 (7)*, 939–948. https://doi.org/10.1039/c003630g

(2) Khairy, M.; El-Safty, S. A. Hemoproteins–nickel foam hybrids as effective supercapacitors. *Chem. Commun.* **2014**, 50, 1356-1358. https://doi.org/10.1039/C3CC48155G

(3) Hassen, D.; El-Safty, S. A.; Tsuchiya, K.; Chatterjee, A.; Elmarakbi, A.; Shenashen, M. A.; Sakai, M. Longitudinal hierarchy Co_3O_4 mesocrystals with high-dense exposure facets and anisotropic interfaces for direct-ethanol fuel cells. *Sci. Rep.* **2016**, 6, 4330. https://doi.org/10.1038/srep24330

(4) Hassen, D.; Shenashen, M. A.; El-Safty, S. A.; Selim, M. M.;Isago, H.; Elmarakbi, A.; El-Safty, A.; Yamaguchi, H. Nitrogen-doped carbon-embedded TiO_2 nanofibers as promising oxygen reduction reaction electrocatalysts. *J. Power Sources* **2016**, 330, 292-303. *http://dx.doi.org/10.1016/j.jpowsour.2016.08.140*

(5) Li, S.; Wu, Q.; Zhang, D.; Liu, Z.; He, Y.; Wang, Z. L.; Sun, C. Effects of pulse charging on the performances of lithium-ion batteries. *Nano Energy* **2019**, *56*, 555–562. https://doi.org/10.1016/j.nanoen.2018.11.070

(6) Armand, M.; Tarascon, J. M. Issues and challenges facing rechargeable lithium batteries. *Nature* **2001**, *414 (6861)*, 359–367. https://doi.org/10.1038/35104644

(7) Aravindan, V.; Sundaramurthy, J.; Kumar, P. S.; Shubha, N.; Ling, W. C.; Ramakrishna, S.; Madhavi, S. A novel strategy to construct high performance lithium-ion cells using one

dimensional electrospun nanofibers, electrodes and separators. *Nanoscale* **2013**, *5 (21)*, 10636–10645. https://doi.org/10.1039/c3nr04486f

(8) Khalifa, H.; El-Safty, S.A.; Shenashen, M.A.; Reda, A.; Elmarakbi. A. Large-scale giant architectonic electrodes designated with complex geometrics and super topographic surfaces for fully cycled dynamic LIB modules. *Energy Storage Mater.* **2020**, *26*, 260-275. https://doi.org/10.1016/j.ensm.2019.12.009

(9) Zhang, W.; Fu, Y.; Liu, W.; Lim, L.; Wang, X.; Yu, A. A General approach for fabricating 3D MFe_2O_4 (M=Mn, Ni, Cu, Co)/graphitic carbon nitride covalently functionalized nitrogen-doped graphene nanocomposites as advanced anodes for lithium-ion batteries. *Nano Energy* **2019**, *57*, 48–56. https://doi.org/10.1016/j.nanoen.2018.12.005

(10) Liu, Y.; Liu, J.; Wang, J.; Banis, M. N.; Xiao, B.; Lushington, A.; Xiao, W.; Li, R.; Sham, T. K.; Liang, G.; Sun, X. Formation of size-dependent and conductive phase on lithium iron phosphate during carbon coating. *Nat. Commun.* **2018**, *9 (1)*, 1–8. https://doi.org/10.1038/s41467-018-03324-7

(11) Zhang, M.; Garcia-Araez, N.; Hector, A. L. Understanding and development of olivine $LiCoPO_4$ cathode materials for lithium-ion batteries. *J. Mater. Chem. A* **2018**, *6 (30)*, 14483–14517. https://doi.org/10.1039/c8ta04063j

(12) Padhi, A. K. Phospho-olivines as positive-electrode materials for rechargeable lithium batteries. *J. Electrochem. Soc.* **1997**, 144 (4), 1188. https://doi.org/10.1149/1.1837571

(13) Khalifa, H.; El-Safty, S.A.; Reda, A.; Shenashen, M.A.; Elmarakbi. A.; Metawa, H.A. Structurally folded curvature surface models of geodes/agate rosettes (cathode/anode) as

vehicle/truck storage for high energy density lithium-ion batteries. *Batteries Supercaps* **2020**, *3 (1)*, 76-92. https://doi.org/10.1002/batt.201900083

(14) Phan, A. T.; Gheribi, A. E.; Chartrand, P. Modelling of phase equilibria of $LiFePO_4$ -$FePO_4$ olivine join for cathode material. Can. J. Chem. Eng. **2018**, 97(8), 1–31. https://doi.org/10.1002/cjce.23416

(15) Yan, X.; Sun, D.; Wang,Y.; Zhang, Z.; Yan, W.; Jiang, J.; Ma, F.; Liu, J.; Jin, Y.; Kanamura, K. The enhanced electrochemical performance of $LiMn_{0.75}Fe_{0.25}PO_4$ nanoplates from multiple interface modification by using fluorine-doped carbon coating**.** *ACS Sustainable Chem. Eng.* **2017**, *5, 6, 4637-4644. https://doi.org/10.1021/acssuschemeng.6b03163*

(16) Kobayashi, S.; Kuwabara, A.; Fisher, C. A. J.; Ukyo, Y.; Ikuhara, Y. Microscopic mechanism of biphasic interface relaxation in lithium iron phosphate after delithiation. *Nat. Commun.* **2018**, *9 (1)*, 1–10. https://doi.org/10.1038/s41467-018-05241-1

(17) Jin, Y.; Tang, X.; Wang, Y.; Dang, W.; Huang, J.; Fang, X. High-tap density $LiFePO_4$ microsphere developed by combined computational and experimental approaches. *CrystEngComm* **2018**, *20 (42)*, 6695–6703. https://doi.org/10.1039/C8CE00894A

(18) Jiang, Y.; Tian, R.; Liu, H.; Chen, J.; Tan, X.; Zhang, L.; Liu, G.; Wang, H.; Sun, L.; Chu, W. Synthesis and characterization of oriented linked $LiFePO_4$ nanoparticles with fast electron and ion transport for high-power lithium-ion batteries. *Nano Res.* **2015**, *8 (12)*, 3803–3814. https://doi.org/10.1007/s12274-015-0879-7

(19) Guo, L.; Zhang, Y.; Wang, J.; Ma, L.; Ma, S.; Zhang, Y.; Wang, E.; Bi, Y.; Wang, D.; McKee, W. C.; Xu Y.; Chen, J.; Zhang, Q.; Nan, C.; Gu, L.; Bruce, P. G.; Peng, Z. Unlocking the energy

capabilities of micron-sized $LiFePO_4$. *Nat. Commun.* **2015**, *6*. https://doi.org/10.1038/ncomms8898

(20) Xiao, J.; Wan, L.; Yang, S.; Xiao, F.; Wang, S. Design hierarchical electrodes with highly conductive $NiCo_2S_4$ nanotube arrays grown on carbon fiber paper for high-performance pseudocapacitors. *Nano Letters* **2014**, *14*, *2*, 831-838. https://doi.org/10.1021/nl404199v

(21) Shenashen, M. A.; Hassen, D.; El-Safty, S. A.; Isago, H.; Elmarakbi, A.; Yamaguchi, H. Axially oriented tubercle vein and X-crossed sheet of N-Co_3O_4@C hierarchical mesoarchitectures as potential heterogeneous catalysts for methanol oxidation reaction. *Chem. Eng. J.* **2017**, 313, 83–98. https://doi.org/10.1016/j.cej.2016.12.003

(22) Liu, H.; Yang, H.; Li, J. A Novel method for preparing $LiFePO_4$ nanorods as a cathode material for lithium-ion power batteries. *Electrochim. Acta* **2010**, *55 (5)*, 1626–1629. https://doi.org/10.1016/j.electacta.2009.10.039

(23) Wagemaker, M.; Ellis, B. L.; Lützenkirchen-Hecht, D.; Mulder, F. M.; Nazar, L. F. Proof of Supervalent Doping in Olivine $LiFePO_4$. *Chem. Mater.* **2008**, *20 (20)*, 6313–6315. https://doi.org/10.1021/cm801781k

(24) Liu, J.; Wang, J.; Yan, X.; Zhang, X.; Yang, G.; Jalbout, A. F.; Wang, R. Long-term cyclability of LiFePO4/carbon composite cathode material for lithium-ion battery applications. *Electrochim. Acta* **2009**, *54 (24)*, 5656–5659. https://doi.org/10.1016/j.electacta.2009.05.003

(25) Qin, G.; Xue, S.; Ma, Q.; Wang, C. The morphology controlled synthesis of 3D networking $LiFePO_4$ with multiwalled-carbon nanotubes for li-ion batteries. CrystEngComm **2014**, 16 (2), 260–269. https://doi.org/10.1039/c3ce41967c

(26) Tian, Z.; Zhou, Z.; Liu, S.; Ye, F.; Yao, S. Enhanced properties of olivine $LiFePO_4$/graphene co-doped with Nb^{5+} and Ti^{4+} by a sol-gel method. *Solid State Ionics* **2015**, *278*, 186–191. https://doi.org/10.1016/j.ssi.2015.06.017

(27) Devaraju, M. K.; Honma, I. Hydrothermal and solvothermal process towards development of LiMPO4 (M = Fe, Mn) nanomaterials for lithium-ion batteries. *Adv. Energy Mater.* **2012**, *2 (3)*, 284–297. https://doi.org/10.1002/aenm.201100642

(28) Qin, X.; Wang, J.; Xie, J.; Li, F.; Wen, L.; Wang, X. Hydrothermally synthesized $LiFePO_4$ crystals with enhanced electrochemical properties: simultaneous suppression of crystal growth along [010] and antisite defect formation. *Phys. Chem. Chem. Phys.* **2012**, *14 (8)*, 2669–2677. https://doi.org/10.1039/c2cp23433e

(29) Li, L.; Wang, L.; Zhang, X.; Xie, M.; Wu, F. and Chen. R. Structural and electrochemical study of hierarchical $LiNi_{1/3}Co_{1/3}Mn_{1/3}O_2$ cathode material for lithium-ion batteries. *ACS Appl. Mater. Interfaces*, **2015**, *7, 39*, 21939-21947. https://doi.org/10.1021/acsami.5b06584

(30) Park, K. S.; Son, J. T.; Chung, H. T.; Kim, S. J.; Lee, C. H.; Kang, K. T.; Kim, H. G. Surface modification by silver coating for improving electrochemical properties of LiFePO4. *Solid State Commun.* **2004**, *129 (5)*, 311–314. https://doi.org/10.1016/j.ssc.2003.10.015

(31) Andersson, A. S.; Kalska, B.; Häggström, L.; Thomas, J. O. Lithium extraction/insertion in $LiFePO_4$: An x-ray diffraction and moessbauer spectroscopy study. *Solid State Ionics* **2000**, *130 (1)*, 41–52. https://doi.org/10.1016/S0167-2738(00)00311-8

(32) Zhang, J.; Lu, J.; Bian, D.; Yang, Z.; Wu, Q. and Zhang. W. Solvothermal synthesis of hierarchical $LiFePO_4$ microplates with exposed (010) faces as cathode materials for lithium ion batteries. *Ind. Eng. Chem. Res.* **2014**, *53, 31*, 12209-12215. https://doi.org/10.1021/ie501743b

(33) Liu, J.; Lin, X.; Han, T.; Li, X.; Gu, C.; and Li, J. A novel litchi-like $LiFePO_4$ sphere/reduced graphene oxide composite Li-ion battery cathode with high capacity, good rate-performance and low-temperature property. *Appl. Surface Sci.* **2018**, *459*, 233–241. https://doi.org/10.1016/j.apsusc.2018.07.199

(34) Yang, Y.; Bai, Y.; Zhao, S.; Chang, Q.; Zhang, W. Electrochemical Performances of Si/TiO2composite Synthesized by Hydrothermal Method. J. Alloys Compd. **2013**, 579, 7–11. https://doi.org/10.1016/j.jallcom.2013.05.023

(35) Chen, J.S.; Archer, L.A. and Lou. X.W. Electrochemical Properties of SnO_2 hollow structures and TiO_2 nanosheets for lithium-ion batteries. *J. Mater. Chem.*, **2011**, *21*, 9912-9924. https://doi.org/10.1039/C0JM04163G

(36) Wang, J.; Bai, Y.; Wu, M.; Yin, J.; Zhang, W. F. Preparation and electrochemical properties of TiO_2 hollow spheres as an anode material for lithium-ion batteries. *J. Power Sources* **2009**, *191 (2)*, 614–618. https://doi.org/10.1016/j.jpowsour.2009.02.056

(37) Lee, D.-H.; Lee, B.-H.; Sinha, A. K.; Park, J.-H.; Kim, M.-S.; Park, J.; Shin, H.; Lee, K.-S.; Sung, Y.-E.; Hyeon, T. Engineering titanium dioxide nanostructures for enhanced lithium-ion storage. *J. Am. Chem. Soc.* **2018**, *140 (48)*, 16676–16684. https://doi.org/10.1021/jacs.8b09487

(38) Chen, B.; Meng, Y.; Sha, J.; Zhong, C.; Hu, W. and Zhao. N. Preparation of MoS_2/TiO_2 based nanocomposites for photocatalysis and rechargeable batteries: progress, challenges, and perspective. *Nanoscale*, **2018**, *10*, 34-68. https://doi.org/10.1039/C7NR07366F

(39) Dambournet, D.; Belharouak, I.; Amine, K. Tailored preparation methods of TiO_2 anatase, rutile, brookite: Mechanism of formation and electrochemical properties. *Chem. Mater.* **2010**, *22 (3)*, 1173–1179. https://doi.org/10.1021/cm902613h

(40) Park, S.; Lee, C.W.; Kim, J.C.; Song, H.J.; Shim H.W.; Lee, S. and Kim, D.W. Heteroepitaxy-induced rutile VO_2 with abundantly exposed (002) facets for high lithium electroactivity. *ACS Energy Letters* **2016**, *1*, *1*, 216-224. https://doi.org/10.1021/acsenergylett.6b00147

(41) Armstrong, G.; Armstrong, A. R.; Canales, J.; Bruce, P. G. Nanotubes with the TiO_2-B structure. *Chem. Commun. 2005*, *19*, 2454–2456. https://doi.org/10.1039/b501883h

(42) Li, Q.; Zhang, J.; Liu, B.; Li, M.; Liu, R.; Li, X.; Ma, H.; Yu, S.; Wang, L.; Zou, Y.; Li, Z.; Zou, B.; Cui, T.; Zou, G. Synthesis of high-density nanocavities inside TiO_2-B nanoribbons and their enhanced electrochemical lithium storage properties. *Inorg. Chem.* **2008**, *47 (21)*, 9870–9873. https://doi.org/10.1021/ic800758d

(43) Soares, A.; Fraisse, B.; Morato, F.; Ionica-Bousquet, C. M.; Monconduit, L. On the synthesis conditions for tailoring lithium composition in ramsdellite phases: Application for Li-ion batteries. *J. Power Sources* **2012**, *208*, 440–446. https://doi.org/10.1016/j.jpowsour.2011.12.013

(44) Pérez-Flores, J. C.; Baehtz, C.; Kuhn, A.; García-Alvarado, F. Hollandite-Type TiO_2: A New negative electrode material for sodium-ion batteries. *J. Mater. Chem. A* **2014**, *2 (6)*, 1825–1833. https://doi.org/10.1039/c3ta13394j

(45) Delogu, F.; Mechanistic, a. study of TiO_2 anatase-to-rutile phase transformation under mechanical processing conditions. *J. Alloys Compd.* **2009**, *468 (1–2)*, 22–27. https://doi.org/10.1016/j.jallcom.2008.01.035

(46) Xiaoyan, P.; Yi, C.; Xueming, M.; Lihui, Z. Phase transformation of nanocrystalline anatase powders induced by mechanical activation. *J. Am. Ceram. Soc.* **2004**, *87 (6)*, 1164–1166. https://doi.org/10.1111/j.1551-2916.2004.01164.x

(47) Aravindan, V.; Lee, Y. S.; Yazami, R.; Madhavi, S. TiO_2 polymorphs in "rocking-chair" Li-ion batteries. *Mater. Today* **2015**, *18 (6)*, 345–351. https://doi.org/10.1016/j.mattod.2015.02.015

(48) Khalifa, H.; El-Safty, S.A.; Reda, A.; Shenashen, M.A.; Selim, M.M.; Elmarakbi. A.; Metawa, H.A. Theoretical and experimental sets of choice anode/cathode architectonics for high-performance full-scale lib built-up models. *Nano-Micro Letters* **2019**, *11 (1)*, 84. https://doi.org/10.1007/s40820-019-0315-8

(49) Khalifa, H.; El-Safty, S.A.; Reda, A.; Selim, M.M.; Elmarakbi. A.; Metawa, H.A.; Shenashen, M.A. Multifaceted geometric 3D mesopolytope cathodes and its directional transport gates for superscalable LIB models. *Appl. Mater. Today*, **2020**, *19*, 100590. https://doi.org/10.1016/j.apmt.2020.100590

(50) Khalifa, H.; El-Safty, S.A.; Reda, A.; Shenashen, M.A.; Selim, M.M.; Alothman, O.Y.; Ohashi, N. Meso/macroscopically multifunctional surface interfaces, ridges, and vortex-modified anode/cathode surfaces as force-driven modulation of high-energy density of LIB electric vehicles. *Sci. Rep.* **2019**, *9 (1)*, 1-17. https://doi.org/10.1038/s41598-019-51345-z

(51) Zhang, J.; Lu, J.; Bian, D.; Yang, Z.; Wu, Q.; Zhang, W. Solvothermal synthesis of hierarchical $LiFePO_4$ microplates with exposed (010) faces as cathode materials for lithium ion batteries. *Ind. Eng. Chem. Res.* **2014**, *53 (31)*, 12209–12215. https://doi.org/10.1021/ie501743b

(52) Jiang, Z.; Jiang, Z. J. Effects of carbon content on the electrochemical performance of LiFePO 4/C core/shell nanocomposites fabricated using $FePO_4$/polyaniline as an iron source. *J. Alloys Compd.* **2012**, *537*, 308–317. https://doi.org/10.1016/j.jallcom.2012.05.066

(53) Zhang, W.; Zhou, X.; Tao, X.; Huang, H.; Gan, Y.; Wang, C. In Situ Construction of Carbon Nano-Interconnects between the $LiFePO_4$grains Using Ultra Low-Cost Asphalt. *Electrochim. Acta* **2010**, *55 (8)*, 2592–2596. https://doi.org/10.1016/j.electacta.2009.11.072

(54) Khalifa, H.; El-Safty, S. A.; Reda, A.; Eid, A.; Elmarakbi, A.; Shenashen, M. A. Mesoscopic open-eye core–shell spheroid carved anode/cathode electrodes for fully reversible and dynamic lithium-ion battery models, *Nanoscale Adv.* **2020**, *2*, 3525-3541 https://doi.org/10.1039/D0NA00203H

(55) Khalifa, H.; El-Safty, S.A.; Reda, A.; Shenashen, M.A.; Eid A.I. Anisotropic alignments of hierarchical Li_2SiO_3/TiO_2@nano-C anode//$LiMnPO_4$@nano-C cathode architectures for full-cell lithium-ion battery. *Nat. Sci. Rev.* **2020**, *7 (5)*, 863-880. https://doi.org/10.1093/nsr/nwaa017

TOC

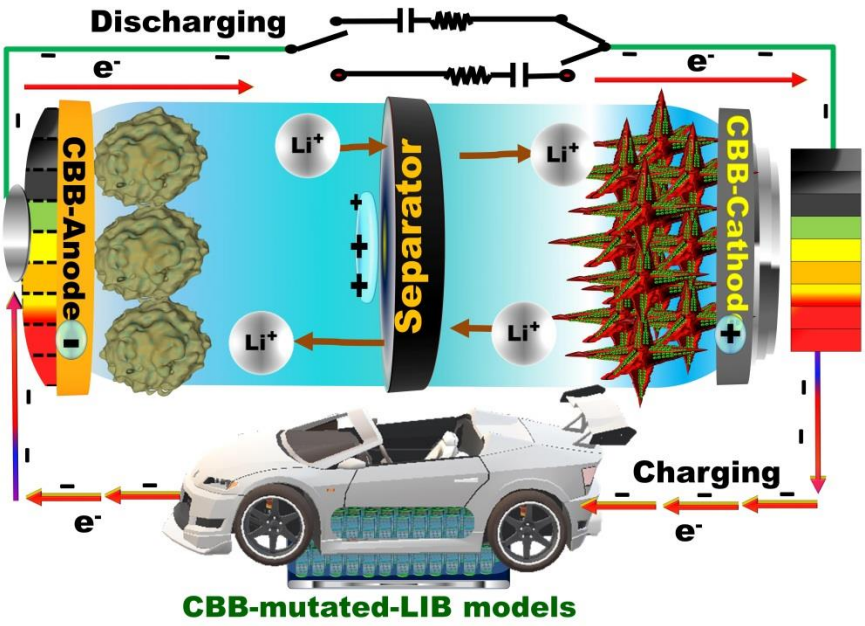

The CBB anode/cathode electrode architectonics designed with multiple complex hierarchies, including uni-, bi-, and tri-modal morphologies, multi-directional configurations, geometrical assemblies oriented in nano-/micro-scale structures, and surface mesh topologies leverage potential fabrication of sustainable full-scale coin-type, and pouch-type LIB models.